Monthly Notices of the ROYAL ASTRONOMICAL SOCIETY

MNRAS **509,** 2362–2376 (2022) https://doi.org/10.1093/mnras/stab2812
Advance Access publication 2021 October 2

Minute-cadence observations of the LAMOST fields with the TMTS: I. Methodology of detecting short-period variables and results from the first-year survey

Jie Lin ,[1]★ Xiaofeng Wang,[1,2]★ Jun Mo,[1]★ Gaobo Xi,[1] Jicheng Zhang,[3] Xiaojun Jiang,[4] Jianrong Shi,[4,5] Xiaobin Zhang,[4] Xiaoming Zhang,[4] Zixuan Wei,[1] Limeng Ye,[6] Chengyuan Wu,[1] Shengyu Yan,[1] Zhihao Chen,[1] Wenxiong Li,[7] Xue Li,[1] Weili Lin,[1] Han Lin,[1] Hanna Sai,[1] Danfeng Xiang[1] and Xinghan Zhang[1]

[1]*Physics Department and Tsinghua Center for Astrophysics, Tsinghua University, Beijing 100084, China*
[2]*Beijing Planetarium, Beijing Academy of Sciences, Beijing 100044, China*
[3]*Department of Astronomy, Beijing Normal University, Beijing 100875, China*
[4]*National Astronomical Observatories of China, Chinese Academy of Sciences, Tsinghua University, Beijing 100012, China*
[5]*School of Astronomy and Space Science, University of Chinese Academy of Sciences, Beijing 100049, China*
[6]*School of Physics and Astronomy, Queen Mary University of London, G. O. Jones Building, 327 Mile End Road, London E1 4NS, UK*
[7]*The School of Physics and Astronomy, Tel Aviv University, Tel Aviv 69978, Israel*

Accepted 2021 September 22. Received 2021 September 15; in original form 2021 July 20

ABSTRACT

Tsinghua University-Ma Huateng Telescopes for Survey (TMTS), located at Xinglong Station of NAOC, has a field of view up to 18 deg^2. The TMTS has started to monitor the LAMOST sky areas since 2020, with the uninterrupted observations lasting for about 6 h on average for each sky area and a cadence of about 1 min. Here, we introduce the data analysis and preliminary scientific results for the first-year observations, which covered 188 LAMOST plates ($\approx$ 1970 deg^2). These observations have generated over 4.9 million uninterrupted light curves, with at least 100 epochs for each of them. These light curves correspond to 4.26 million *Gaia*-DR2 sources, among which 285 thousand sources are found to have multi-epoch spectra from the LAMOST. By analysing these light curves with the Lomb–Scargle periodograms, we identify more than 3700 periodic variable star candidates with periods below $\approx$7.5 h, primarily consisting of eclipsing binaries and δ Scuti stars. Those short-period binaries will provide important constraints on theories of binary evolution and possible sources for space gravitational wave experiments in the future. Moreover, we also identified 42 flare stars by searching rapidly evolving signals in the light curves. The densely sampled light curves from the TMTS allow us to better quantify the shapes and durations for these flares.

Key words: surveys – binaries: close – stars: flare – stars: oscillations (including pulsations).

1 INTRODUCTION

The binaries with orbital periods shorter than a few hours, namely ultracompact binaries (UCBs), play a crucial role in the functional tests of space gravitational wave (GW) observatories (Shah, van der Sluys & Nelemans 2012). Over the past 2 yr, the Zwicky Transient Facility (ZTF) has discovered a few UCBs with orbital period shorter than 20 min through densely sampled photometric measurements (Burdge et al. 2019, 2020a, b), these binaries are predicted to be detected by LISA with high signal to noise (SNR) and to aid their GW parameter estimation. On the other hand, as a class of binary with the shortest orbital period, UCBs represent the terminal phase of some binary evolution, which provide opportunities in studying physics under extreme conditions and give crucial constraints on the binary evolution, such as mass-accretion/loss processes, common-envelope evolution, and angular-momentum loss mechanisms (see also Rappaport, Verbunt & Joss 1983; Zhu, Lü & Wang 2012; Toonen, Voss & Knigge 2014; Chen, Liu & Wang 2020b; Wang et al. 2021).

Non-interacting black hole binaries (or candidates), which cannot be detected by current X-ray detectors, have been discovered by periodic photometric variability and radial velocities (RVs) of their visible companion stars (Liu et al. 2019; Thompson et al. 2019). Furthermore, some newest researches suggest that the black holes in the short-period ellipsoidal variables can be revealed by analysing the Fourier amplitudes of their light curves (Gomel, Faigler & Mazeh 2021a, b; Gomel et al. 2021c). As the cross field between GW verification binaries and black hole binaries, the ultracompact black hole (X-ray) binaries (Bahramian et al. 2017), in which the X-ray radiation should be inefficient (Menou, Narayan & Lasota 1999; Knevitt et al. 2014), are expected to be first discovered by high-cadence, wide-area optical survey missions or next-generation GW observatories. The ultracompact black hole binaries could be the unique Galactic black hole systems that can be detected by both

★ E-mail: wang_xf@mail.tsinghua.edu.cn (XW); linjie2019@mail.tsinghua.edu.cn (JL); mojun@mail.tsinghua.edu.cn (JM)

gravitational and electromagnetic waves, implying they will be the most direct evidence that the stellar black hole exists.

So far, a dozen of ground-based survey missions have operated to search for transients and variables on different time-scales. These missions include the Deep Lens Survey (DLS, 1999–2005; Becker et al. 2004), the Faint Sky Variability Survey (FSVS; Groot et al. 2003), the RApid Temporal Survey (RATS; Ramsay & Hakala 2005), the Catalina Real Time Survey (CRTS, since 2007; Drake et al. 2009, 2014b, c), the Palomar Transient Factory (PTF, 2009–2012; Law et al. 2009; Rau et al. 2009), the omegaWhite survey (Macfarlane et al. 2015), the Intermediate Palomar Transient Factory (iPTF, 2013–2017; Ho et al. 2018; Chatterjee et al. 2019), the High Cadence Transient Survey (HiTS; Martínez-Palomera et al. 2018), the Evryscope (since 2015; Ratzloff et al. 2019), the ZTF (since 2017; Bellm et al. 2019; Masci et al. 2019), the Compact binary HIgh CAdence Survey (CHiCaS; Pala et al. 2020a). High-cadence surveys, especially uninterrupted time series photometry, are more efficient in discovering short-period light variations and phenomenon associated with stellar flares/bursts. However, only a few missions (e.g. ZTF high-cadence Galactic Plane Survey; Kupfer et al. 2021) insist on performing uninterrupted photometry, as high-cadence surveys will significantly sacrifice the coverage of the sky area. Fortunately, several space-based survey missions, such as the *Kepler* mission (Borucki et al. 2010; Koch et al. 2010) and the *Transiting Exoplanet Survey Satellite* (*TESS*; Ricker et al. 2014, 2015), have operated to perform long-duration uninterrupted photometry. However, *Kepler* was limited to observe only Cygnus-Lyra region and ecliptic plane, while *TESS* was designed to monitor the brightest dwarf stars. Moreover, these space-based missions usually suffer low efficiency of data transportation, and thus finally provide light curves for only hundred thousands of objects.

As Burdge et al. (2020a) mentioned, a systematic search and study of UCBs relies not only on the high-cadence photometry, but also on the time-resolved spectroscopy. The high-cadence photometry is used to search for periodic signals, while the spectra are used to determine semi-amplitude of RVs. On the other hand, studies of fast-evolving transients such as flare stars also require spectroscopic confirmation (Kulkarni & Rau 2006; Ho et al. 2018). Therefore, we initiated a new high-cadence survey mission, with an attempt to cover the LAMOST sky areas with the Tsinghua University-Ma Huateng Telescopes for Survey (TMTS; Zhang et al. 2020). The LAMOST has started the time-domain medium-resolution spectroscopic survey since October 2018 (Liu et al. 2020), which provides precise measurements of the RV variations for stars brighter than 15.0 mag.

In this paper, we present the methods of data analysis and preliminary results for the first-year high-cadence surveys from the TMTS. The schema of first-year observations and light-curve data set are described in Section 2. The descriptions of photometry and calibration are presented in Section 3. In Section 4, we introduce the methodology of detecting variability, periodicity, and flares in the TMTS light curves, respectively. In this section, we also describe the source selection with the Hertzsprung–Russell (HR) diagram. We present some selected results in Section 5.

2 OBSERVATION

TMTS is a multiple-tube telescope system consisting of four 40-cm optical telescopes with a total field of view (FoV) of about 18 $\deg^2$ (4.5 $\deg^2$ for each telescope) and a plate scale of 1.86 arcsec pixel^{-1}. The TMTS system is equipped with 4096 × 4096 pixels CMOS cameras, which have short read-out time (<1 s) and allow to conduct high-cadence photometry for targets on large sky areas. Detailed introduction about the performance of TMTS is described in Zhang et al. (2020).

Since TMTS and LAMOST have similar FoV and locate at the same site (i.e. Xinglong Station of NAOC), the former is an ideal telescope system to carry out collaborative tasks with the latter. At Xinglong Station, the typical seeing is better or comparable to 2.6 arcsec for 80 per cent of nights and the sky brightness at zenith is around 21.1 mag arcsec^{-2} (Huang et al. 2012; Zhang et al. 2015). Due to the light pollution from the surrounding cities, the sky brightness increases with the increase of zenith angle. As Zhang et al. (2015) introduced, 32 per cent of nights in Xinglong Station have cloud-free observations for at least 6 h, which means that about 117 nights per year are suitable for the interrupted photometric observations required by the TMTS.

The TMTS has two observation modes: (i) staring at the LAMOST areas for the whole night whenever possible with a cadence of about 1 min; (ii) supernova survey with a cadence of about 1–2 d. In this paper, we concentrate on the first-year observations of the LAMOST sky areas. In order to achieve a high SNR, the observations are conducted in Luminous filter (L filter hereafter), which has a very wide coverage ranging from 330 nm to about 900 nm when combined with the CMOS detector (see fig. 6 in Zhang et al. 2020). Similar to *Gaia*'s G band (330–1050 nm; Gaia Collaboration 2018), the 'white-light' band can maximize the detection depth of optical telescopes. For a 1-min exposure, the 3σ detection limit of the TMTS can reach about 19.4 mag.

As shown in Fig. 1, the TMTS observed 188 LAMOST plates during the whole year of 2020, covering a total sky area of $\approx$ 1970 $\deg^2$. Among them, the sky area of $\approx$1793 $\deg^2$ has at least 100 uninterrupted 1-min exposures, as shown in the left-hand panel of Fig. 2. Notice that, the 1-min image here is combined from six 10-s images and its frame rate thus dropped to $\approx$1/75 Hz. For the purpose of selecting variables based on the light-curve analysis (LCA), we focus on the observed sky areas with at least 100 epochs, which take up about 96 per cent of the LAMOST sky areas monitored during the first year. The high-cadence survey allows us to discover and identify variables in the LAMOST fields on a time-scale of about 1 min.

As can be seen from the right-hand panel of Fig. 2, the TMTS has produced $\approx$13 million uninterrupted light curves during the survey conducted in 2020, of which $\approx$6 million have at least 100 repeated measurements. Notice that there are about 4.7 million light curves with less than 20 epochs. The sources with such sparse measurements could locate either near the edge of FoV or hover around the detection limit. Based on the light curves with at least 100 'valid' measurements (see details in Section 3), we built a data set including 4.9 million selected light curves from the first-year survey, namely **TMTS-ULC1st** data set. It is worth noting that, multiple light curves may correspond to the same source due to that some sources are located in the overlapping FoV of multiple telescopes of TMTS. Since each light curve can be used to detect variability and periodicity for a source independently and only a small part of sources have multiple light curves, the repeated light curves are not spliced together.

3 PHOTOMETRY AND CALIBRATION

All of the 10-s raw images from the TMTS are first bias-, dark-, and flat-corrected using the *fitsh* package (Pál 2012). Then the astrometric calibration is applied to the 10-s single frame using the soft package *scamp* (Bertin 2006) and the reference catalogue of PPM-Extended (PPMX; Röser et al. 2008). The *scamp* can automatically generate accurate World Coordinate System (WCS) information by cross-correlating the reference catalogue, and it

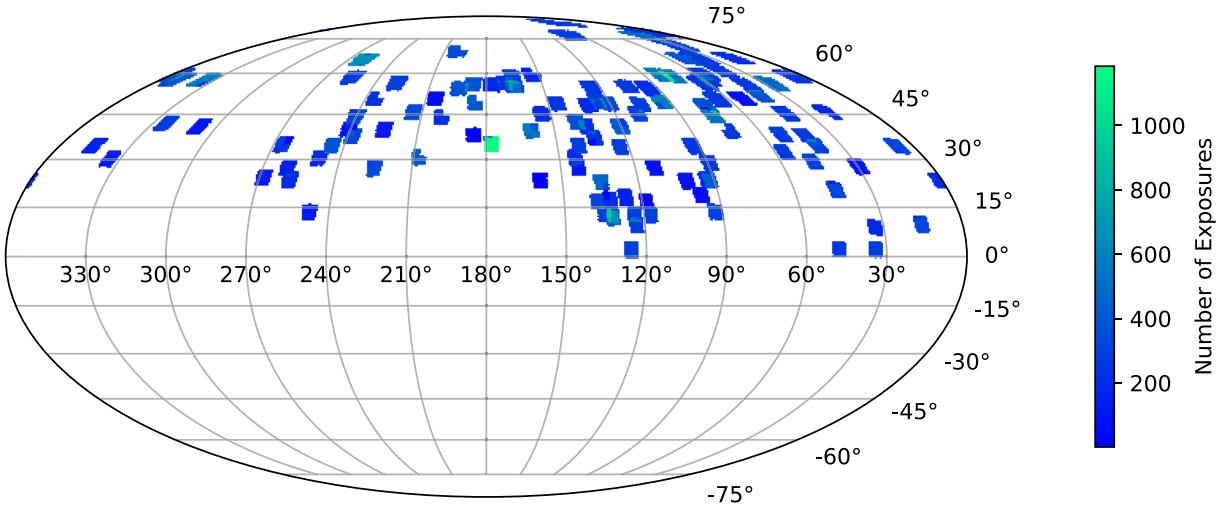

Figure 1. Observation sky areas of the TMTS shown in equatorial coordinates. The sky map is plotted by using the HEALPIX package (http://healpix.sourceforge.net) with NSIDE = 128 (Górski et al. 2005). The depth of the colour represents the total number of 1-min exposure.

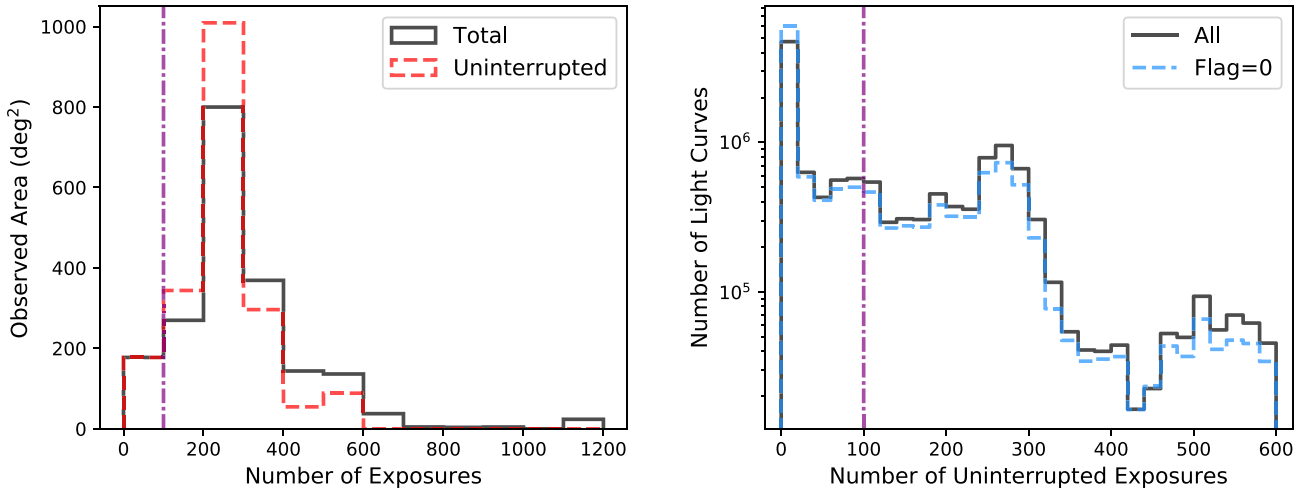

Figure 2. Histogram of number of (1-min) exposures for observed area (left) and light curves (right). *Left:* The black solid line and red dashed line represent the statistics based on overall and uninterrupted observations, respectively. The purple dot–dashed lines indicate the cut-off value (i.e. 100 repeated exposures). *Right:* The blue dashed line represents the exposure number of valid measurements (i.e. flag=0; see details in Section 3).

can give accurate astrometric solutions for the FITS images. To improve the detection depth, six successive single frames are median combined into a 1-min image using the soft module *SWarp* in the *TERAPIX* pipeline (Bertin et al. 2002). We extract the fluxes of sources on the combined images using the soft package Source Extractor (*SExtractor*; Bertin & Arnouts 1996).

We checked the *SExtractor* flag for all of the TMTS measurements. The *SExtractor* flag $\neq 0$ means that there are some problems in the measurements, e.g. blending or saturation (see details in https://sextractor.readthedocs.io/en/latest/Flagging.html). In addition, we added a new flag bit (value = 256) to mark the measurements within 100 pixels of the detector boundary, as these measurements frequently cause spurious variations in the light curves and are difficult to be calibrated. Due to immature manufacturing process, the backgrounds of four regions divided by the X/Y midlines in the CMOS detector are not completely consistent, especially during big moon nights (see Zhang et al. 2020). This inconsistency would cause spurious variation in the light curves of objects across the midlines, we thus added an additional flag bit (value = 512) to those detections within 40 pixels of the detector midlines. The histogram of flag = 0 measurements ('valid measurements' hereafter) is also shown in the right-hand panel of Fig. 2, and the number of light curves with at least 100 repeated valid measurements is ≈4.9 million.

The flux measurements from continuous observations were combined into a light curve. Before detecting real variability and periodicity, we need to first remove the systematic effects like spurious variations caused by changes in airmass, lunar phase, and solar altitude, etc. The *Tamuz*'s method (Tamuz, Mazeh & Zucker 2005) and the principal component analysis (PCA) are not adopted in the analysis. Because the extinction coefficients in these algorithms cannot be correctly determined for variable stars, as these methods actually make an assumption that the magnitudes of each light curve are equal to its average. Some methods can better constrain the coefficients for variable stars but a prior model on the intrinsic variation needs to be assumed (see also Ofir et al. 2010; Aigrain et al. 2017). For these reasons, we developed a weighted version of 'differential photometry' to reduce the systematic errors of the light curves. Similar to the *Tamuz*'s method and PCA, our algorithm

adopted in the analysis also involves removing the common trends and features among a large set of light curves. These common trends and features can be modelled by (weighted) averaging all measurements for constant stars (i.e. the stars that show no variations during the observations) within the FoV. The 'effective extinction coefficient' for each star (i.e. c_i in Tamuz et al. 2005) is not set in our algorithm, since the coefficient cannot be determined accurately for those variable stars. Instead, a weighted factor based on the separations between reference stars of constant luminosity and target object is introduced to modulate various effects in different detection regions. Hence, the corrected flux $F_i^{\rm corr}$ at epoch t_i for target source i is calculated as

$$F_i^{\rm corr} = F_i \times \alpha_i = F_i \times \prod_{j=1}^{M} \left(\frac{\overline{F_j^{\rm ref}}}{F_{i,j}^{\rm ref}} \right)^{\omega_j / \sum_{j=1}^{M} \omega_j}, \quad (1)$$

where α_i represents the correction factor and M is the total number of reference stars. F_i and $F_{i,j}^{\rm ref}$ are the uncorrected flux for the target and the jth reference star at time t_i, respectively. $\overline{F_j^{\rm ref}}$ is the average uncorrected flux of the jth reference star over an observation night, and it is expressed as $\sum_{i=1}^{N} F_{i,j}^{\rm ref}/N$, where N is the number of epochs. The ω_j is a weighted factor for the jth reference star, which is set to 1 arcsec$^2/(a_j + C)^2$, where a_j is the separation between the target and the jth reference star. The characteristic separation C is set to be a small value (i.e. 60 arcsec in our work) to avoid the singular value when the reference star is very close to the target. The corrected fluxes seem to be insensitive to the value of C and the results are not significantly different even if the characteristic separation C is set as 10 arcmin.

The sources with 13 mag $< G <$ 17 mag were selected to be the reference star candidates, the G represents the mean G-band magnitudes from *Gaia* DR2 data base (Gaia Collaboration 2016, 2018). In order to improve the calibration process, we only adopted the reference star candidates with $q = 100$ per cent for their light curves, where $q = N(\text{flag} = 0)/N$ is a parameter to evaluate the quality of a light curve. N indicates the total number of epochs for a given light curve and $N(\text{flag} = 0)$ represents the number of valid measurements. Notice that, the reference stars may contain some variables which should be revealed and kicked out through iterative process. In order to reveal those variables in the reference stars, we calculated the inverse von Neumann ratio for all of our light curves (see Shin, Sekora & Byun 2009; Sokolovsky et al. 2017). This ratio is a very useful variability index derived by testing the independence of successive measurements. The inverse von Neumann ratio (Sokolovsky et al. 2017) is defined as

$$\frac{1}{\eta} = \frac{\sum_{i=1}^{N} \left(F_i^{\rm corr} - \overline{F^{\rm corr}} \right)^2}{\sum_{i=1}^{N-1} \left(F_{i+1}^{\rm corr} - F_i^{\rm corr} \right)^2}, \quad (2)$$

where $\overline{F^{\rm corr}}$ represents the corrected flux averaged over all epochs. We set a very tight cut-off value, i.e. 0.8, to exclude all variables from the reference stars. We will explain why $\frac{1}{\eta} = 0.8$ is a robust threshold in Section 4.1.

An example of re-calibrated flux and correction factor for the TMTS light curve of a WUMa-type eclipsing binary (i.e. CRTS J075625.0+420405) are shown in the top and middle panels of Fig. 3, respectively. To obtain the corresponding magnitudes, we also calculate the magnitude zero-point m_0 for each target, which

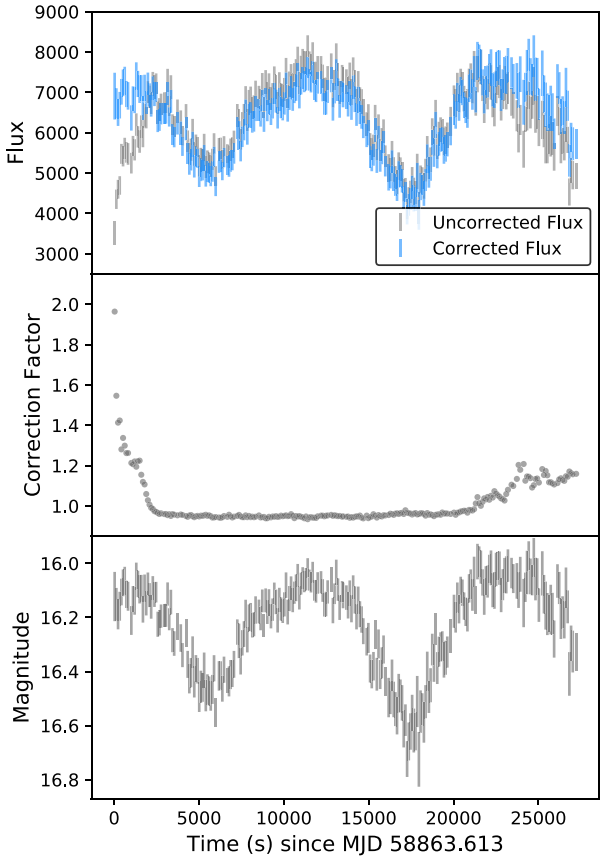

Figure 3. Example of TMTS light curve and correction factor (i.e. the α_i in equation 1) for the W UMa-type eclipsing binary CRTS J075625.0+420405 (Drake et al. 2014a; Marsh et al. 2017), which was observed by the telescope #3 of TMTS for ≈5.3 h on 2020 January 15.

follows as

$$m_0 = \frac{\sum_{j=1}^{M} \omega_j \times \left(2.5 \log_{10} \overline{F_j^{\rm ref}} + G_j \right)}{\sum_{j=1}^{M} \omega_j}, \quad (3)$$

where G_j is the *Gaia* DR2 G magnitude of the jth reference star. The magnitude obtained at epoch t_i is thus estimated as $m_i = -2.5 \times \log_{10} F_i^{\rm corr} + m_0$. Inserting equations (1) and (3) into the above equation, the magnitude can be expressed as

$$m_i = \frac{\sum_{j=1}^{M} \omega_j \times \left(-2.5 \log_{10} \frac{F_i}{F_{i,j}^{\rm ref}} + G_j \right)}{\sum_{j=1}^{M} \omega_j}. \quad (4)$$

The bottom panel of Fig. 3 shows the final magnitudes obtained with the TMTS for CRTS J075625.0+420405. It is worth noting that, the measurement accuracy of TMTS is superior to the space-based survey mission *TESS*, as shown by the comparison of the light curves obtained for the same source (see Fig. 4).

Fig. 5 shows the comparison of TMTS magnitudes obtained in L band with the G magnitudes from *Gaia* DR2. The mean TMTS magnitudes here were taken from the light curves of TMTS-ULC1st. The corresponding *Gaia* sources with reliable parallax measurements ($\sigma_\varpi/\varpi \leq 0.2$ here, where ϖ is the parallax and σ_ϖ represents the error of parallax) are used to cross-match the TMTS sources. One can

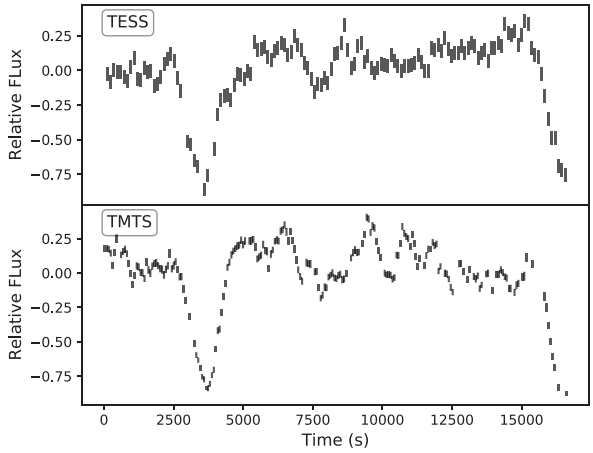

Figure 4. A comparison between *TESS* and TMTS light curves. The observed object is HS 0455+8315, which is an eclipsing cataclysmic variable (CV) with a visual magnitude from about 15 to 17 (Downes et al. 2001). TMTS observed this object on 2020 November 2, and the *TESS* (PDC) light curve was obtained from the observations on 2020 June 9 (Sector 26). The start time of *TESS* light curve is reset to make its major eclipse coincide with that of TMTS.

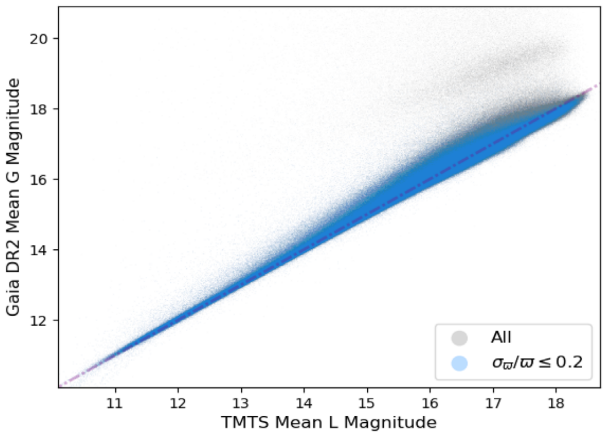

Figure 5. Comparison of TMTS L-band magnitudes with *Gaia* DR2 G-band Magnitude. The blue points represent the sources with reliable parallax measurements ($\sigma_{\varpi}/\varpi \leq 0.2$), which means that these sources have more precise astrometric solutions. The purple dot–dashed line represents the diagonal line.

see that TMTS L magnitudes are basically consistent with the *Gaia* G magnitudes while the scatter between these two magnitude systems tends to increase at the faint end (see the blue points in Fig. 5). Notice that the *Gaia* sources with spurious parallax values (e.g. negative value) are usually faint and likely locate in crowded regions (e.g. low Galactic latitude) where their astrometric solutions are poorly constrained (Gaia Collaboration 2018). For the comparison, we also showed an overall version that includes the sources with spurious astrometric measurements (see the grey points in Fig. 5), these sources with poor astrometry from *Gaia* caused an additional cluster above the original distribution when matching with the TMTS sources, which also appeared in the comparison between *Gaia* DR1 G magnitudes and DR2 G magnitudes (see details in https://gea.esac.esa.int/archive/documentation/GDR2/index.html).

4 METHODS

4.1 Variability detection

Difference image analysis (DIA; Tomaney & Crotts 1996; Alard & Lupton 1998) and LCA (Sokolovsky et al. 2017) are two main methods to search for variables. Compared with the DIA, the LCA, based on the measurements obtained at more than two epochs, can reveal low-amplitude variability. In search for variable sources from the TMTS light curves, we calculated two common variability indices. As it is difficult to detect reliable variabilities for the light curves covering a very short duration, we thus identified variable sources for those light curves with at least 100 valid epochs (see also Gomel et al. 2021c; Kupfer et al. 2021).

We selected the TMTS light curves of the TMTS-ULC1st data set (≈4.9 million) with instrumental magnitude $11.0 < \widetilde{m} < 18.5$. Since the average zero-point of all measurements is 25.59 ± 0.25, we defined the instrumental magnitude as $\widetilde{m} = -2.5 \times \log_{10}(\overline{F^{\rm corr}}) + 25.6$. The value of the instrumental magnitude here is close to but not equal to the astrophysical magnitude, due to that the variations of photometric zero points with sky areas and observation conditions are not considered.

The upper panel of Fig. 6 shows the histogram of number of TMTS light curves from the TMTS-ULC1st data set as a function of the instrumental magnitude. From magnitude 12 to 17, the number density of TMTS light curves increases by about an order of magnitude. The highest number density appears at $\widetilde{m} \approx 17.0$ mag. At the fainter end, the number density is limited by the varied detection depths; at the brighter end, the detections suffer from effects of both saturation and small number of bright stars.

We have calculated the robust standard deviation (StD) and inverse von Neumann ratio ($1/\eta$ here) as a function of their instrumental magnitude $\widetilde{m}$ for the selected TMTS light curves (see the middle and lower panels of Fig. 6). The robust StD is the standard deviation inferred from the central 50 percentile of the data points by assuming a Gaussian distribution (Ofek et al. 2020), implying that the robust StD is extremely insensitive to outliers or occasional variations. The normalized robust StD, defined as the ratio of the robust StD to the median flux, increases from ∼0.01 to ∼0.1 when the brightness of the sources decreases from 12 to 18 mag. Those points that have significantly larger 'scatter' than the expected are very likely due to light variations. We use fifth-order polynomial to fit the median and the 10σ excess, respectively, which are both calculated in a bin of 0.1 mag. There are about 5600 light curves that have higher robust Std than the 10σ threshold (the blue square in the middle panel of Fig. 6). These light curves correspond to about 5300 *Gaia* DR2 sources. However, it is difficult to conclude that these sources are all astrophysically variable stars, since blended sources can also show variabilities in their light curves. For example, Kupfer et al. (2021) recently revealed a false positive rate (i.e. the rate of non-astrophysically variable sources) of up to 85 per cent for the variability detection in the high-cadence Galactic Plane observations of ZTF. By visually inspecting 300 TMTS light curves with significance of light variations being above the 10σ threshold, we found that non-astrophysically variable stars accounted for about 67 per cent. For a lower threshold, i.e. 5σ, about 23 000 light curves can be selected but the false positive rate increases to about 86 per cent. Obviously, the lower thresholds can be used to pick more astrophysically variable stars, but the higher false positive rates also result in a huge sample containing more non-astrophysically variable sources that is hard to be visually inspected. Therefore, we will take the variability

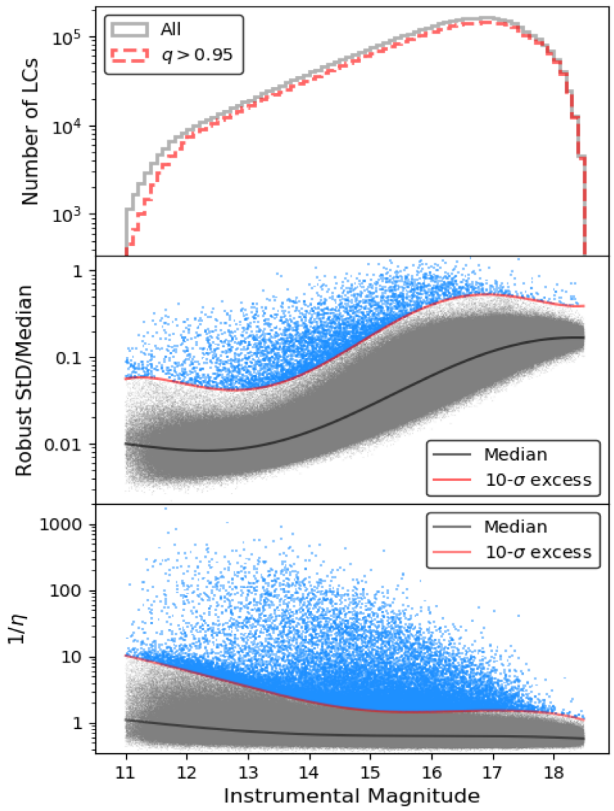

Figure 6. Distribution of light curves, robust Std and inverse von Neumann ratio versus the instrumental magnitude. *Upper panel*: Distribution of the number of the TMTS light curves from the TMTS-ULC1st data set against the magnitudes. The red dashed line represents the light curves with quality higher than 95 per cent (see Section 3). The bin size of the histogram is 0.1 mag. *Middle panel*: The normalized robust StD versus the magnitude. The black and red solid lines represent the polynomial fit to the median and 10σ threshold, respectively. The blue squares indicate those light curves with variability index being above the 10σ threshold. *Lower panel*: The inverse von Neumann ratio versus the magnitude.

indices as an auxiliary condition to select periodic variables and flare stars.

The inverse von Neumann ratio quantifies the smoothness of a time-series successive variation and does not depend on the uncertainty of the measurements as the contribution of uncertainty has been nearly offset by its denominator as shown in equation (2). For an ideal time series of photometry following a Gaussian distribution, the expected value of its $1/\eta$ is equal to 0.5. However, for real photometric measurements, which do not follow the Gaussian distribution or are not completely independent of each other, the cut-off value should be determined based on the distribution of $1/\eta$ (see Sokolovsky et al. 2017). Given the characteristics of $1/\eta$, we use a third-order polynomial (rather than the fifth-order polynomial) to fit the median and robust StD versus $\widetilde{m}$, respectively, which yields ≈24 000 light curves showing variations beyond the 10σ threshold. Notice that the $1/\eta$ does not obey the Gaussian distribution in practise, hence the 'σ' here does not represent the confidence level corresponding to Gaussian distribution. Moreover, we found that $1/\eta$ tends to be larger for brighter sources, which could be caused by the unmarked saturations. The saturation effect tends to reduce the independence of successive measurements and thus increase the value of $1/\eta$.

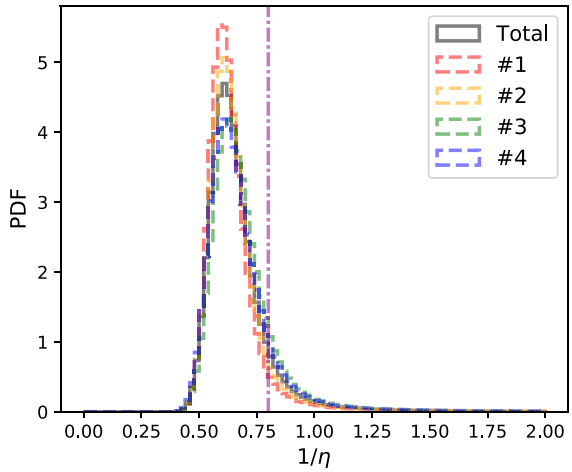

Figure 7. Density distribution of inverse von Neumann Ratio $1/\eta$ of light curves from the TMTS-ULC1st data set for the all four (grey solid line) and each of four (colourful dashed line) telescopes of TMTS. The bin size here is 0.02. The purple dot–dashed line indicates the cut-off value to determine the non-variable reference sources for photometric calibration.

For the purpose of excluding all variable stars from the reference stars, we use $1/\eta$ to identify variable sources because the robust StD parameter is insensitive to the occasional variations (e.g. the variations of flare stars). Since the threshold of variability index varies with the instrumental magnitude, we thus defined a statistic parameter $\epsilon_{\frac{1}{\eta}} = [\frac{1}{\eta} - \nu(\widetilde{m})]/\sigma(\widetilde{m})$, where $\nu(\widetilde{m})$ and $\sigma(\widetilde{m})$ are the median and robust standard deviation of inverse von Neumann ratios for the TMTS light curves at a given magnitude, respectively. The $\epsilon_{\frac{1}{\eta}}$ is a key parameter to introduce the significance of variability for a light curve.

As introduced above, although the identifications of astrophysically variable stars using the variability indices have a low true positive rate (TPR), they can be used to identify stars of constant luminosity at a very high TPR since the light variations caused by image quality will not increase the FPR of non-variable sources. The setting of the thresholds for variability indices is usually arbitrary (see Bellm et al. 2019; Kupfer et al. 2021; Nidever et al. 2021). In the photometric calibration process (shown in Section 3), a fixed threshold $1/\eta \leq 0.8$ is empirically set to identify non-variable sources. It is a tight threshold that ensures $\epsilon_{\frac{1}{\eta}} \lesssim 1.5$ for the reference stars in all observed magnitudes, corresponding to the exclusion of about 12 per cent of the reference star candidates.

Furthermore, we compare the density distribution of inverse von Neumann ratio for each telescope of the TMTS system. As Fig. 7 shows, the $1/\eta$ distribution of each telescope is roughly consistent with each other except that the telescope #1 and telescope #2 have a slightly more concentrated distribution, implying that the capability of variability detection is almost equivalent for each telescope. Therefore, the same threshold for variability indices is adopted for all of the four telescopes.

4.2 Periodicity detection

Due to potential non-uniform sampling caused by some 'bad' measurements, we test the periodicity of TMTS light curves using the Lomb–Scargle periodogram (LSP hereafter; Lomb 1976; Scargle

1982; VanderPlas 2018). The LSP here is defined as

$$P(f) = \frac{1}{2\sigma^2} \times \left\{ \frac{\left[\sum_{i=1}^{N} F_i \times \cos\, 2\pi f(t_i - \tau)\right]^2}{\sum_{i=1}^{N} \cos^2\, 2\pi f(t_i - \tau)} + \frac{\left[\sum_{i=1}^{N} F_i \times \sin\, 2\pi f(t_i - \tau)\right]^2}{\sum_{i=1}^{N} \sin^2\, 2\pi f(t_i - \tau)} \right\},$$

$$\text{and } \tau = \frac{1}{4\pi f} \times \left(\arctan \frac{\sum_{i=1}^{N} \sin\, 4\pi f t_i}{\sum_{i=1}^{N} \cos\, 4\pi f t_i} \right), \quad (5)$$

where F_i is the flux at epoch t_i after the calibration (see Section 3), f is the test frequency, and σ^2 is the variance of the fluxes. The LSP here is normalized by the variance and thus the white noise in LSP follows the exponential distribution as $\exp(-z)$ (see also Coughlin et al. 2020). We determine the most likely photometric period by searching the highest LSP peak $P_{\max}$ in the frequency range of $3/2T \leq f \leq f_{\rm nyq}$, where T is the time span of the observations and $f_{\rm nyq}$ is the (pseudo-)Nyquist frequency (VanderPlas 2018), which can be estimated as a half of average sampling rate ($\approx$1/75 Hz). Notice that, the observations must cover one and half cycles before we can determine its periodicity.

Based on the cumulative distribution function (CDF) of $\exp(-z)$ and the multiplicative property of the independent probabilities, the false alarm probability (FAP; see Lomb 1976) of periodicity can be estimated as

$$\text{FAP} = 1 - [1 - \exp(-P_{\max})]^{N_{\rm eff}}, \quad (6)$$

where $N_{\rm eff}$ is the number of independent frequencies, which can be calculated by $N_{\rm eff} = f_{\rm nyq} T$ in approximation (VanderPlas 2018), namely a half of total number of epochs. Notice that the estimate of FAP is completely dependent on the assumption of white noise. However, LSP power tends to be higher at lower frequency because of the effect of red noise, thus the resultant FAP could be seriously underestimated, especially at the low-frequency end. Due to relatively short duration of our continuous photometry, the LSP is more likely to be polluted by the red noise generated from non-periodic or long-period variations. Therefore, we also search for the high LSP powers at lower frequency range (i.e. $f < 3/2T$), since strong powers in the low-frequency range (as $P^{\rm red}$) are very likely caused by red noise rather than real periodic behaviour. All light curves with $P^{\rm red} > P_{\max}$ were marked to indicate the possible red noises in the LSPs. Several samples of period search are shown in Fig. 8. Noted that both panel *ii-b* and panel *v-b* have higher powers $P^{\rm red}$ below the frequency threshold, implying that they suffered non-periodic variations during the observations.

For the purpose of checking the periodicity FAPs obtained from the light curves in the TMTS-ULC1st data set, we plotted their CDF in Fig. 9. For comparison, we also generated 10 000 simulated time series, and each is composed of random 100–1000 points that obey a normal distribution. As shown in Fig. 9, the periodicity FAPs, calculated from these simulated time series, follows exactly the ideal null distribution 1−CDF=FAP. This implies that the method of obtaining periodicity FAPs is feasible if the TMTS measurements are independent and follow a Gaussian distribution. However, our FAP, estimated from real data set, deviates significantly from the ideal null distribution. Such a deviation was also found to exist in the data set of other survey mission (Drake et al. 2013, 2014a). It is known that the detectable periodic variable stars take only a small percentage of all observed sources (Drake et al. 2014a, 2017; Chen et al. 2020a; Ofek et al. 2020), the periodicity FAP discussed here can be seriously underestimated in practise.

In order to derive more reliable estimate of periodicity FAPs, some methods have been developed, such as the *Baluev*'s method (Baluev 2008) and bootstrap method (Ivezić et al. 2014). As an alternative, we construct a true null distribution by real data set since we have already calculated the FAPs for all available light curves of the TMTS-ULC1st data set. By assuming that most observed sources are non-periodic sources (typically $\gtrsim$ 90 per cent) and periodic sources tend to have higher LSP peaks and thus lower FAPs, we can take the highest 90 per cent FAPs as approximated null samples. We found these null samples (corresponding to the 1−CDF>0.1 part of grey solid line in Fig. 9) follow a straight line in the logarithmic 1−CDF versus logarithmic FAP diagram, implying that the null distribution of real data may differ from the ideal null distribution by only a constant k, namely $\log_{10}(1 - \text{CDF}) = k \times \log_{10}\text{FAP}$. By fitting the distribution of these null samples, we obtained $k = 0.225$ for all light curves of the TMTS-ULC1st data set and then the modified false alarm probabilities can be expressed as $\text{FAP}_{\rm mod} = \text{FAP}^k$. Notice that the k value actually varies for different data sets as the performance of flux measurements is dependent on the observation conditions. Thus, a 'daily' k value is determined from daily observation data set in real time and 'daily' modified FAPs are generated for the light curves.

The distribution of modified FAP is shown in Fig. 10, where one can see that the area between the grey line and blue line corresponds to the candidates of periodic variable. About 99 per cent TMTS light curves [i.e. $\log_{10}(1 - \text{CDF}) > -2$] match the ideal null distribution, implying that the (detectable) periodic light curves account for only a few thousandths of TMTS-ULC1st data set. Notice that, due to the limitation of current observation duration (typically within a night), it is difficult to reveal long-period variables (e.g. $P > 0.5$ d; see details in Section 5.1) using the TMTS-ULC1st data set. But the number of periodic variables will be greatly improved with the ongoing of supernova survey of TMTS.

4.3 Flare search

A common method of flare detection is to search for outliers in the light curves for which non-flare variations (e.g. large-amplitude and long-duration variations) have been removed. For the purpose of avoiding false flares caused by instrumental errors or cosmic rays, the flare search often requires at least two consecutive outliers rather than one-point outliers (Walkowicz et al. 2011; Osten et al. 2012; Yang et al. 2018). In order to remove the non-flare variations, Osten et al. (2012) use two different models to fit periodic and non-periodic light curves, respectively. To avoid the comparison of goodness for two models and speed up the data analysis, we fit all light curves by a unified compound model of fourth-order Fourier series (Pojmanski 2002; Drake et al. 2014a, 2017; Kim & Bailer-Jones 2016) and second-order polynomial. The polynomial terms here are used to offset the potential long-scale variations. Notice that the purpose of fitting here is to remove the non-flare variations, rather than modelling the true variations of light curves. The compound model is expressed as

$$F_i^{\rm model} = \sum_{j=0}^{2} c_i \times t_i^j + \sum_{k=1}^{4} a_k \times \cos(2\pi\, k\, f_{\max}\, t_i) + b_k \times \sin(2\pi\, k\, f_{\max}\, t_i), \quad (7)$$

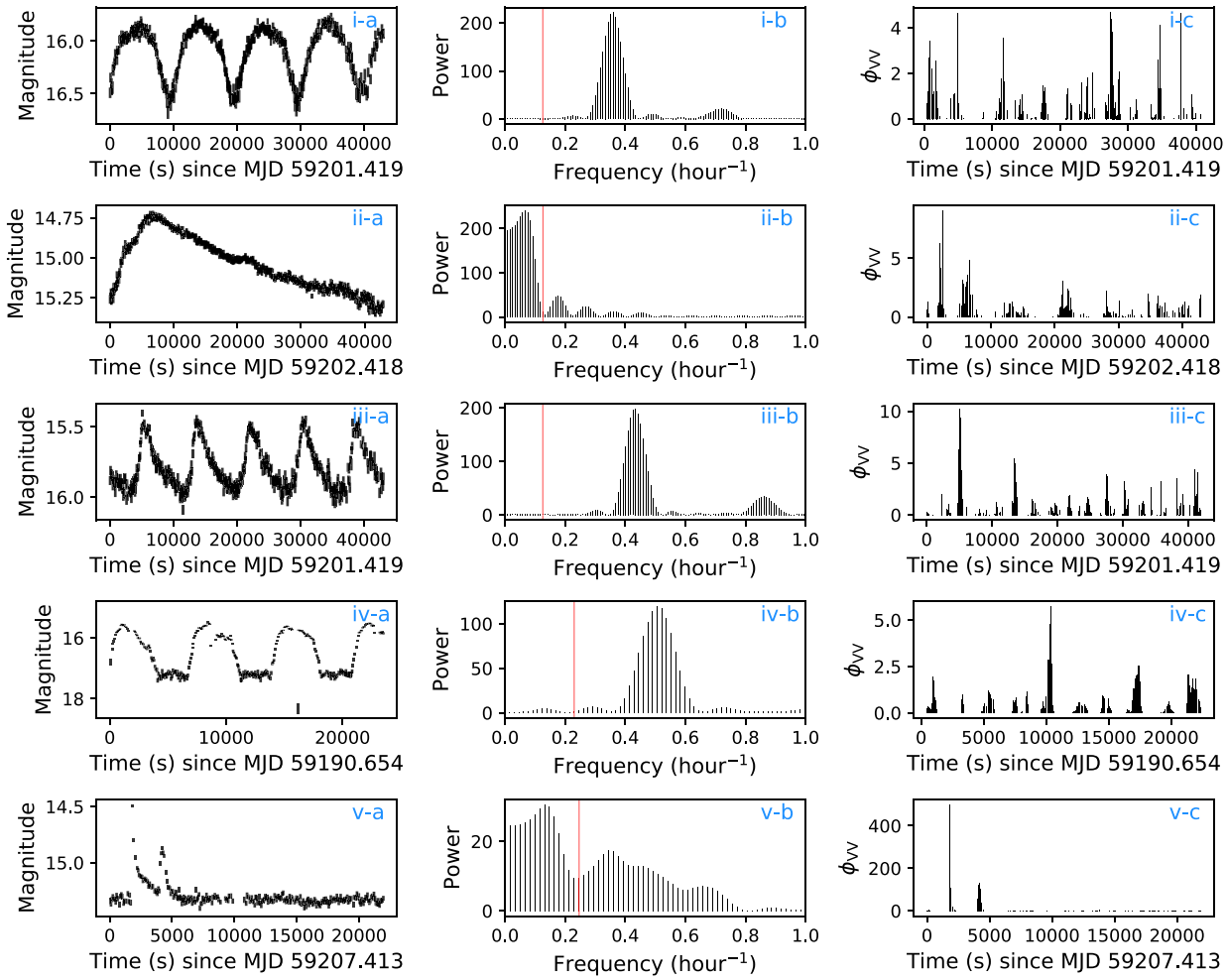

Figure 8. Examples for detections of periodicity variables and flare stars. The row *i* to *v* correspond to a W UMa-type eclipsing binary, an RR Lyr-type variable, a δ Scuti star, an AM Her-type CV, and a multipeak flare, respectively. Columns *a*, *b*, and *c* represent the TMTS light curves, LSPs, and time series of ϕ_{VV}, respectively. The red lines in column *b* represent the frequency threshold (i.e. 3/2*T*) used to investigate the red noise in LSPs. Notice that, the LSPs here are a zoom-in version, the complete LSPs cover the frequency even higher than 20 h^{-1}.

where f_{max} is the frequency corresponding to the highest power P_{max} in the LSP (see Section 4.2). Notice that even if a light curve is non-periodic, we can still find a f_{max} in its LSP. For such a light curve, our model is still applicable while the values of best-fitting a_k and b_k are very small.

The residual flux $F_i^{res} = F_i - F_i^{model}$ can be easily obtained and the normalized residual could be calculated as

$$r_i = \frac{F_i^{res} - \overline{F^{res}}}{\sigma^{res}}, \tag{8}$$

where $\overline{F^{res}}$ and σ^{res} represent the median flux and the robust standard deviation of residual fluxes, respectively. It is worth noting that, we adopted the robust StD instead of the uncertainty in flux measurements, since the former can reveal true scatter in the residual fluxes. In this way, the normalized residuals (except the points corresponding to flares) will obey a normal distribution, which is the prerequisite to estimate the significance of selected flare candidates.

The flare candidates are selected by locating the maximum ϕ_{VV} in a time series (Osten et al. 2012), where the ϕ_{VV} is defined as the product of continuous two normalized residuals,

$$\phi_{VV,i} = r_i \times r_{i+1}. \tag{9}$$

The examples of flare search using time series of ϕ_{VV} are also shown in Fig. 8, where one can see that only the row *v* (corresponding to a flare) has very strong ϕ_{VV} values in its time series.

To estimate the false discovery rate (FDR), some studies (Kowalski et al. 2009; Osten et al. 2012; Paudel et al. 2018, 2020) have applied the FDR analysis following Miller et al. (2001). However, the *Miller*'s method is not applied to our project, because it requires a large number of null samples manually selected from the data set of light curves, but this work cannot be finished automatically in real time by our pipeline. Therefore, we explored the mathematical formula for the null distribution of ϕ_{VV}.

As introduced above, the (non-flare) normalized residual fluxes obey a normal distribution. By assuming successive residuals are independent of each other, the product of two normalized residuals (i.e. ϕ_{VV}) should follow the probability density function (PDF) as indicated below,

$$\mathrm{PDF} = \frac{K_0(|\phi_{VV}|)}{\pi} = \frac{1}{\pi}\int_0^{\infty} \frac{\cos(\phi_{VV}\, t)}{\sqrt{t^2+1}}\, \mathrm{d}\, t, \tag{10}$$

where K_0 is the special ($n = 0$) case of *modified Bessel function of the second kind* (Abramowitz & Stegun 1972). Fig. 11 shows the density distribution of about 36 million ϕ_{VV} measurements from the TMTS

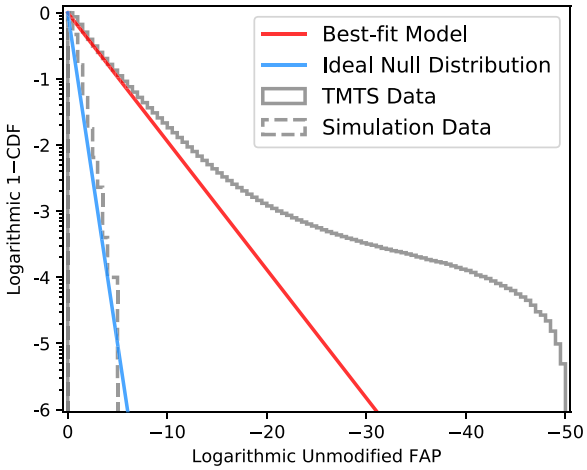

Figure 9. CDF of unmodified FAP for periodicity detection in the TMTS-ULC1st data set. The bin size is 0.5. The grey solid line represents the FAPs obtained from the TMTS-ULC1st light curves, and the red solid line is the model fitted to the grey bins above 1−CDF=0.1. The grey dashed line represents the FAP distribution derived from 10 000 simulated time series obeying a normal distribution, and the blue solid line is the ideal null distribution with 1−CDF=FAP.

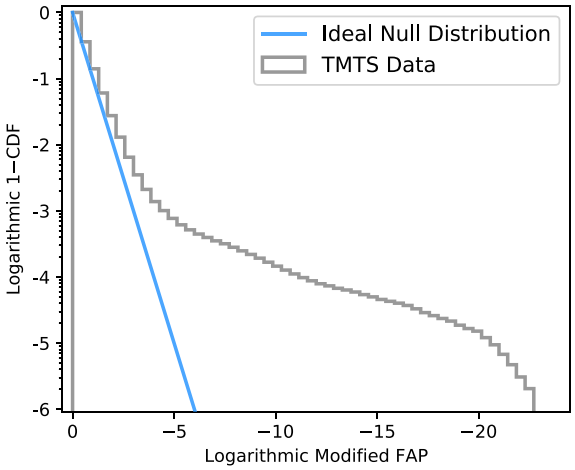

Figure 10. CDF of modified FAP for periodicity detection in the TMTS-ULC1st data set. The bin size is 0.5. The grey solid line represents the FAP modified by $k = 0.225$, and the blue solid line is the ideal null distribution with 1−CDF=FAP.

observation conducted on 2020 December 19. The Bessel function is characterized by the density distribution of $\phi_{\rm VV}$, implying that the CDF of the Bessel function can be applied to estimate the FDR for flare candidates.

Similar to equation (6), the FDR of flares can be estimated as

$$\mathrm{FDR} = 1 - \left[1 - \frac{1}{2\pi}\int_{\phi_{\rm VV,max}}^{\infty} K_0(|x|)\,\mathrm{d}\,x\right]^{N-1}, \quad (11)$$

where $\phi_{\rm VV,\,max}$ is the maximum value of $\phi_{\rm VV}$ inferred in a time series and $N-1$ is the number of $\phi_{\rm VV}$. Notice that, for the purpose of selecting flares, we must exclude the $\phi_{\rm VV}$ derived from the product of a pair of negative r_i values (thus the integral probability term is multiplied by a factor of $\frac{1}{2}$ in equation 11).

The CDF of flare FDRs for about 4.9 million light curves of TMTS-ULC1st data set is shown in Fig. 12. The FDR distribution

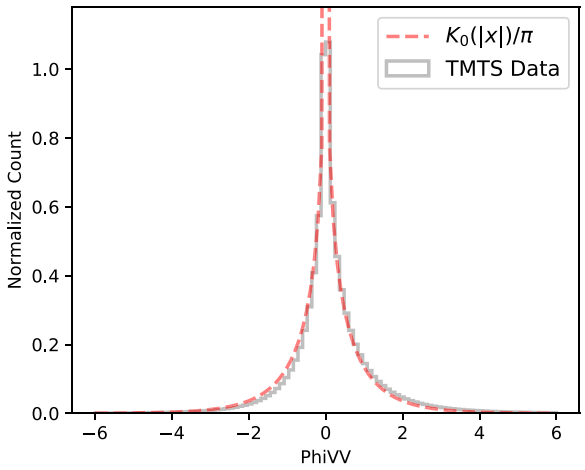

Figure 11. The density distribution of $\phi_{\rm VV}$ calculated from the TMTS observation on 2020 December 19. The observation data include about 36 million $\phi_{\rm VV}$ measurements from light curves of about 82 000 sources. The bin size is 0.06.

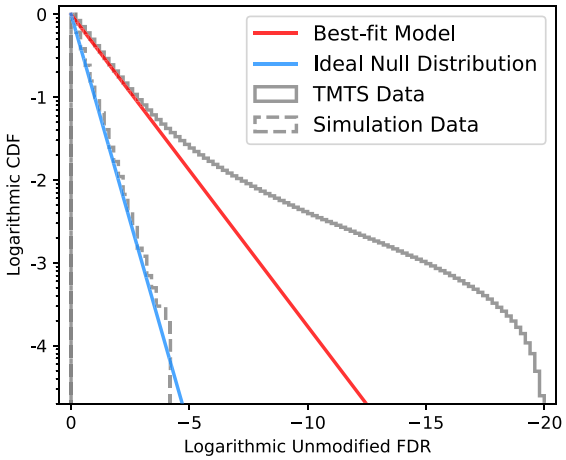

Figure 12. CDF of unmodified FDR for flare detection in the TMTS-ULC1st light curves. The bin size is 0.2.

generated from 10 000 simulated random time series (see more in Section 4.2) matches well with the ideal null distribution, suggesting that our mathematical formula of calculating the FDR is applicable for normally distributed and independent residuals. However, as the successive normalized residuals are not completely independent of each other, the FDRs generated from the TMTS-ULC1st data set deviate significantly from that of the ideal null distribution. Here, we applied the same methods and assumptions described in Section 4.2 to modify the FDR. By fitting the cumulative distribution above 0.1, we obtained $k = 0.376$ for the overall TMTS-ULC1st data and modified the FDR by $\mathrm{FDR_{mod}} = \mathrm{FDR}^k$. On the other hand, for daily observation data set, our pipeline of data analysis will also automatically determine a 'daily' k value, which helps modify the FDR derived from daily observation data in a more accurate way.

4.4 Cross match with other catalogues

In order to obtain additional information (e.g. distance and RV) for source selections, we have cross-matched all of the TMTS sources with the *Gaia* DR2 data base and the LAMOST DR7 (including both low- and medium-resolution spectra) catalogues.

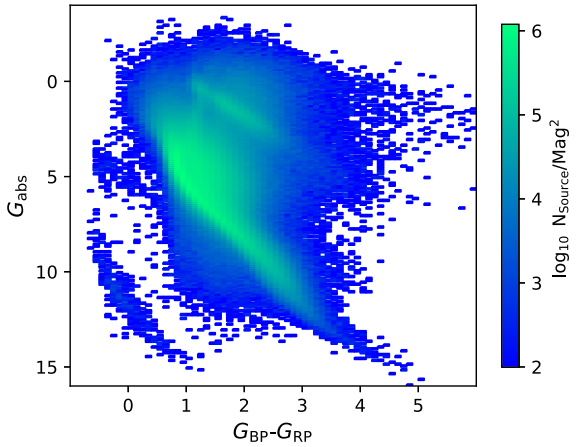

Figure 13. Density distribution of the *Gaia* DR2-TMTS sources across the HR diagram. The bin's size is 0.1 × 0.1 mag^2, and the total number of sources is 2.63 million.

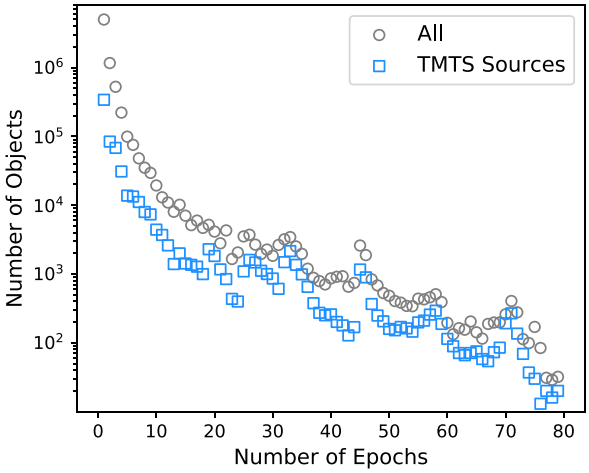

Figure 14. Number distribution of LAMOST DR7 epochs (including both low-resolution and single-exposure medium-resolution spectra). The blue squares represent the distribution for the LAMOST-TMTS sources.

4.4.1 Gaia

The *Gaia* DR2 covers 1.69 billion sources brighter than 21 mag, among which astrometric positions, parallax and proper motion parameters are available for more than 1.33 billion sources (Gaia Collaboration 2018). Most of these sources also have photometric data in G (330–1050 nm), B (330–630 nm), and R bands (630–1050 nm).

Out of the 4.87 million light curves from the TMTS-ULC1st data set, about 4.83 million light curves (99 per cent) are found to have the *Gaia*-DR2 counterparts. The remained sources without *Gaia* counterparts are either transients or bad detections. After removing a part of sources that are located in multiple LAMOST plates or repeatedly observed by different telescopes of TMTS, the total number of the *Gaia*-DR2 counterparts is 4.26 million. Among them, about 4.18 million (98 per cent) *Gaia* sources have parallax measurements, but only 2.63 million (62 per cent) have reliable parallax measurements (i.e. $\sigma_{\varpi}/\varpi \leq 0.2$ here).

Based on parallax, G magnitude and colour ($G_{BP} - G_{RP}$), we can plot the HR diagram for these *Gaia* DR2-TMTS sources, which is a very valid tool to select the white dwarfs (Jiménez-Esteban et al. 2018; Gentile Fusillo et al. 2019; Pelisoli & Vos 2019; Kim, Lépine & Medan 2020) and hot subdwarf stars (Geier et al. 2019; Geier 2020). As shown in Fig. 13, the *Gaia* DR2-TMTS sources cover a wide area across the HR diagram. The reddening corrections were not applied to these sources. The high-density areas in HR diagram correspond to giant stars and main-sequence stars, which include some classes of variables, such as pulsating stars and eclipsing binaries. The TMTS has also captured a small number of white dwarfs in its first-year observations. By applying a simple set of cuts for G_{abs} and $G_{BP} - G_{RP}$ (the equations 2–5 in Gentile Fusillo et al. 2019), we identified 565 (≈0.02 per cent) white dwarf candidates out of the 2.63 million TMTS sources. Furthermore, we can identify CVs (Pala et al. 2020b) and δ Scuti stars in periodic variables (see details in Section 5.1).

4.4.2 LAMOST

From 2011 to 2019, the LAMOST spectroscopic survey has obtained 10.6 million low-resolution ($R \sim 1800$) spectra and 11.4 million single-exposure medium-resolution ($R \sim 7500$) spectra for about 8.9 million LAMOST targets brighter than 17.5 mag (see more in Cui et al. 2012; Zhao et al. 2012; and http://dr7.lamost.org). In the LAMOST DR7 catalogue *v1.2*, all of the LAMOST targets have already been cross-matched with that of the *Gaia* DR2 catalogue.

Plenty of atmospheric parameters (including effective temperature, surface gravity, and metallicity) can be inferred from the observed spectra by applying LAMOST Stellar Parameter pipeline (LASP). The abundant spectral parameters from LAMOST can help identify the variable stars from the TMTS. It is worth noting that, LAMOST can provide RV measurements for millions of stars. These RV measurements were determined by LASP or cross-correlation with KURUCZ synthetic templates (Wang et al. 2019). As multi-epoch spectra are available for millions of objects, the LAMOST data can reveal RV variations for a large number of stars. Hence, the LAMOST data can be used to select those with significant RV variations (e.g. eclipsing binaries; Yang et al. 2020) and even the binaries harbouring an invisible high-mass companion (i.e. black hole binary candidates; Liu et al. 2019; Thompson et al. 2019; Yi, Sun & Gu 2019; Zheng et al. 2019).

Fig. 14 shows the number of objects corresponding to the LAMOST DR7 spectra versus the number of the corresponding spectra that contain both low-resolution and single-exposure medium-resolution spectra. About 2.35 million sources (32 per cent of LAMOST sources) have 2 to over 70 epochs, and the number of sources decrease with the number of epochs. After cross-matching the TMTS sources in TMTS-ULC1st data set with the LAMOST DR7 catalogue, we find that there are 626 000 sources (8.5 per cent of the LAMOST sources) in common. Among them, 285 000 TMTS sources have multi-epoch spectra. For a 5-yr survey, the TMTS is expected to provide high-cadence photometric data for more than half of the LAMOST sources.

5 PRELIMINARY RESULTS

In this section, we present some preliminary results from the first-year high-cadence photometric observations of the LAMOST fields with the TMTS. The result of searching for periodic variable sources is shown in Section 5.1, and the result for flares is shown in Section 5.2.

5.1 Periodic variable sources

The TMTS-ULC1st light curves with periodic variations (typically shorter than 4 h) are selected by the following criteria: (i) 'daily'

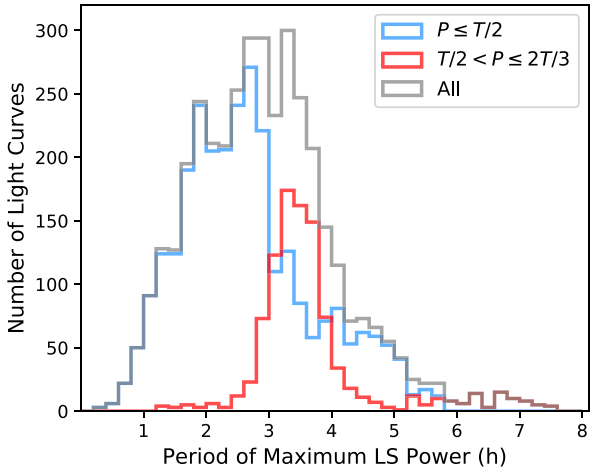

Figure 15. Period distribution of selected light curves from the TMTS-ULC1st data set. The red and blue lines represent the sets of light curves selected with different ratios of period of light variation to observation duration.

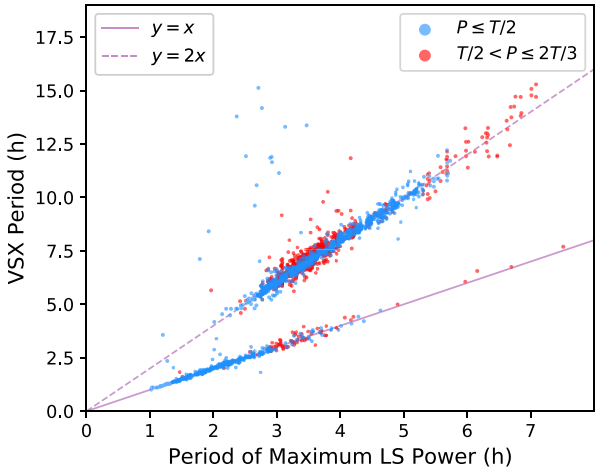

Figure 16. The phase-folded light curves for two shortest-period stars from TMTS-ULC1st. The upper panel shows a δ Scuti star candidate with a period of 18.4 min and an amplitude of 0.03 mag; the lower panel shows a BLAP candidate with a period of 18.9 min and an amplitude of 0.26 mag. Notice that, the BLAP candidate has been observed by telescope #1 (grey) and #3 (red) within different nights, respectively.

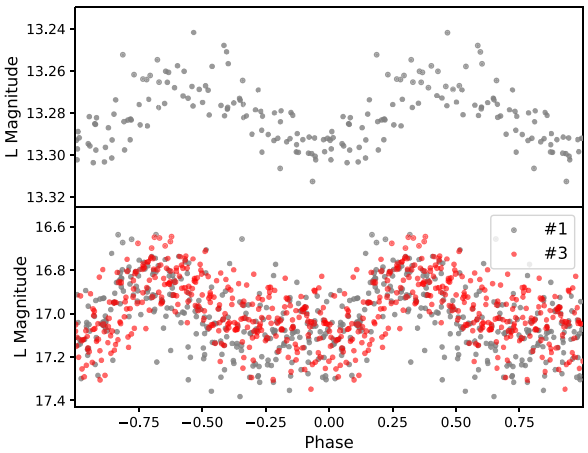

Figure 17. Period of the highest peak in the periodogram from the TMTS-ULC1st data set versus the period given by the International Variable Star Index (VSX). The solid and dashed lines represent the relation $y = x$ and $y = 2x$, respectively.

periodic FAP < 0.001; (ii) no significant Red Noise; (iii) LC quality > 95 per cent. As a result, 6626 light curves were selected. However, these selection criteria may introduce a large number of light curves with false periodic variations due to that a wide periodicity criterion was applied. In order to improve the TPR, we applied two sets of criteria to select the light curves with different ratios of photometric period to observation duration (P/T), respectively. To select light curves that cover at least two complete periods of light variations [i.e. new criterion (iv) $P \leq T/2$], we followed previous selection criteria (i)–(iii). This resulted in 2835 candidate light curves. For the purpose of collecting light curves with periodic variations slightly longer than a half of the observation duration (i.e. $T/2 < P \leq 2T/3$), we adopted the following tighter criteria: (i+) 'daily' periodic FAP $<10^{-5}$; (ii) and (iii) are the same as the previous criteria; (iv+) $T/2 < P \leq 2T/3$; (v) the variability index $\epsilon_{\frac{1}{\eta}} \geq 3.0$ (see details in Section 4.1). With these modified criteria, 988 additional light curves were selected.

The period distribution of all 3823 candidate light curves (corresponding to 3723 *Gaia* DR2 sources) is shown in Fig. 15. The periods of these selected candidates are distributed from about 20 min to 7.5 h (see Fig. 15). The number of candidates increases linearly with the photometric period until it peaks at around 3 h. For the uninterrupted observations, the detectable period is obviously dependent on the observation duration within a night. Although the observation strategy prevents us from discovering longer period variable stars, the number of short-period variables found by TMTS is very competitive (see also Burdge et al. 2020a; Chen et al. 2020a; Ofek et al. 2020). For a 5-yr survey plan, TMTS is expected to reveal more than 20 000 periodic variable stars with period shorter than 8 h.

It is worth noting that, 81 periodic variable star candidates (corresponding to 77 unique sources) have a photometric period below 1 h, as the total number of periodic variable stars with periods below 1 h in the International Variable Star Index (VSX, the version updated on 2021 May 31; Watson, Henden & Price 2006) is only 887. In the next few years, TMTS will greatly expand the sample of ultra-short periodic variable stars. The vast majority of these sources are δ Scuti stars, some blue large-amplitude pulsators (BLAPs; Pietrukowicz et al. 2017) and UCBs are also likely captured. To distinguish the BLAPs and UCBs from the δ Scuti stars, we need to investigate their absolute magnitudes, colours, and spectra. The phase-folded light curves for two shortest-period stars are shown in Fig. 16. Their periods (and amplitudes) are 18.4 min (0.03 mag) and 18.9 min (0.26 mag), respectively. With the *Gaia* $G_{\rm abs}$ and $G_{\rm BP} - G_{\rm RP}$ colour measurements, we inferred that the former is a low-amplitude δ Scuti star while the latter is a BLAP. Further photometric and spectroscopic observations are undergoing. We will study these ultra-short periodic variable stars in separate papers.

All objects of these candidate light curves were cross-matched with the VSX. As a result, 1603 light curves have a VSX counterpart recorded and almost all these counterparts have a period measurement given by VSX. We plotted the period corresponding to the maximum power in TMTS LSP against the VSX period in Fig. 17. The VSX periods basically coincide with the TMTS periods or twice the TMTS periods (typically eclipsing binaries) except for a few inconsistent measurements ($\lesssim 2$ per cent of all samples). These inconsistent measurements are typically caused by multiperiod variable stars or spurious periods in light curves.

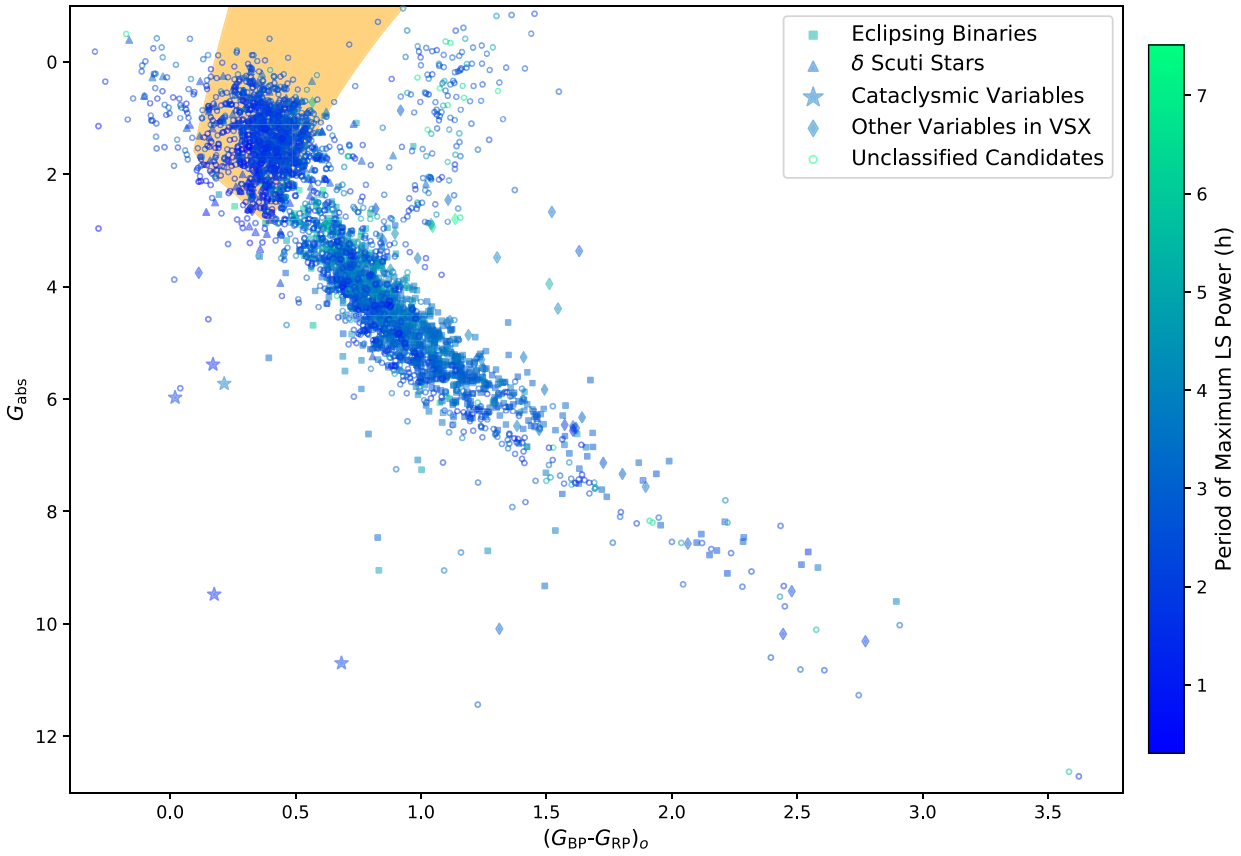

Figure 18. Distribution of periodic variable star candidates across the HR diagram. All points represent the periodic variable star candidates selected from the TMTS-ULC1st data set, among which the eclipsing binaries, δ Scuti stars, CVs, and other variables identified in the International Variable Star Index (VSX) are highlighted using the symbol shape of square, triangle, star, and diamond, respectively. The open circles represent the periodic variable candidates that are not registered in VSX yet. The colour depth of symbols represents the period corresponding to the maximum power in LSP(s). The orange area indicates the instability strip. Notice that, the period corresponding to eclipsing binaries here is the photometric period rather than the orbital period, since these candidates are not completely classified yet.

All objects corresponding to candidate light curves are also cross-matched with the *Gaia* DR2 catalogue. Because some light curves match with repeated sources, all these candidate light curves correspond to **3723** unique *Gaia* sources. Among these stars, **2987** sources have both a $G_{BP} - G_{RP}$ measurement and a reliable parallax measurement. Fig. 18 shows the distribution of these sources across the HR diagram. Both the absolute magnitudes and the colour of these sources were dereddened using the 3D dust map from Green et al. (2019) and the DUSTMAPS PYTHON package[1] (Green 2018). After crosschecking with the latest VSX catalogue, we find that more than half of our periodic variable star candidates are newly discovered. In Fig. 18, we compared these periodic variable star candidates with the δ Scuti instability strip inferred by using the strip boundaries from Murphy et al. (2019) and the evolutionary tracks of single stars from the Podova Stellar Evolution Database (Girardi et al. 2000). As a result, about 940 periodic variable stars were found to locate in the instability strip, among which about 800 candidates could be new-discovered δ Scuti stars. Notice that, the number is still underestimated, as more than 700 candidates have not good parallax measurement and thus cannot be put in the HR diagram. This demonstrates the high efficiency of discovering short-period variables by the TMTS.

[1]https://github.com/gregreen/dustmaps

In comparison, the estimate of the number for eclipsing binaries is more difficult, as the eclipsing binaries distributed on a much wider area of the HR diagram than the δ Scuti stars. Due to the special profiles of light curves from eclipsing binaries, they could be identified by the random forest (RF) or neural networks (NNs). By adopting the cyclic-permutation invariant NNs from Zhang & Bloom (2021), there are about 1900 eclipsing binaries in our 3723 periodic variable star candidates, among which about 600 eclipsing binaries are new-discovered (see details in Xi et al., in preparation). Notice that, the results did not include the eclipsing binaries that were covered by TMTS observations for shorter than 1.5 photometric periods (i.e. 0.75 orbital period). These longer-period eclipsing binaries are expected to be identified by eyes or new algorithm of NNs.

Since about 20 per cent of periodic variable star candidates have not reliable *Gaia* parallax measurements, the identifications of these candidates rely on additional spectroscopic observations. Among 3723 periodic variable star candidates, 1252 sources are observed by the LAMOST and 814 sources have measurements of both surface gravity (log g) measurement and effective temperature (T_{eff}), which means that a part of candidates can be identified using the parameters from the LAMOST spectra. This is because the two dominant classes of short-period variable sources, δ Scuti stars and eclipsing binaries, locate at distinct areas in the T_{eff}–log g diagram (see Fig. 19). With the cut-off temperature 6500 K from Murphy et al. (2019), 290 new δ

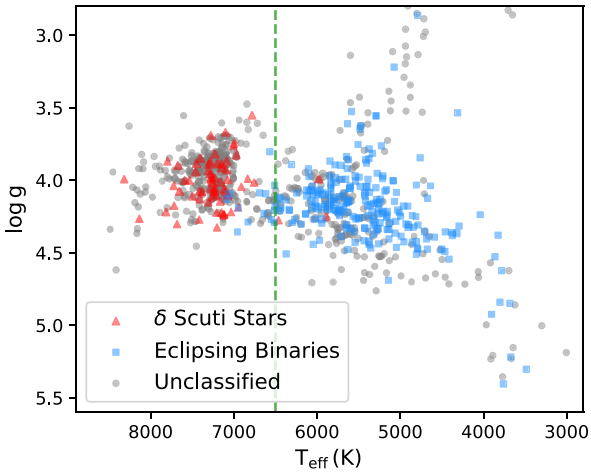

Figure 19. LAMOST surface gravity versus effective temperature for periodic variable candidates from the TMTS-ULC1st data set. The red triangles and blue squares represent the δ Scuti stars and eclipsing binaries identified in VSX, respectively. The unclassified periodic variable candidates are labelled as grey circles. The green dashed line indicates the cut-off temperature for selecting δ Scuti stars (see also Murphy et al. 2019).

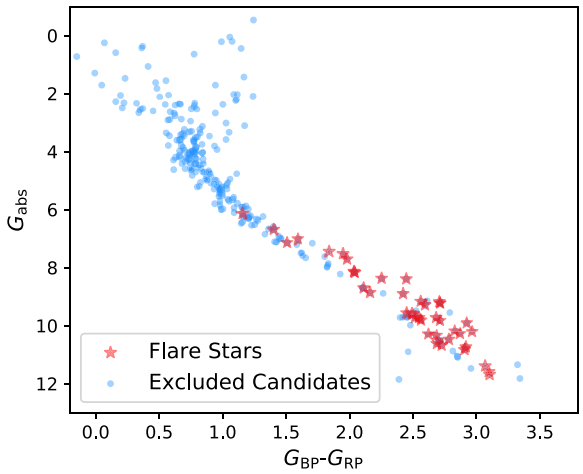

Figure 20. Distribution of the flare stars and candidates in the HR diagram. The confirmed flare stars are labelled with red star symbol.

Scuti star candidates are selected from the 502 unidentified periodic variable candidates, and the remained unidentified candidates are very likely eclipsing binaries.

The LAMOST has started time-domain medium-resolution spectroscopic survey since 2018, and one of the main scientific goals of this survey is to discover quiescent or non-interacting black hole binaries in our Galaxy. Since a few binaries harbouring an invisible high-mass companion (e.g. $M_{\rm unseen} > 3$ M$_\odot$) have been proposed as black hole binary candidates (Gu et al. 2019; Liu et al. 2019; Thompson et al. 2019; Yi et al. 2019; Zheng et al. 2019; Clavel et al. 2021; Gomel et al. 2021c). With multi-epoch RV measurements from the spectroscopic surveys and periodic provided by the wide-field photometric survey missions like TMTS, the lower limits of mass functions are easily estimated for the observed binaries. It is worth noting that, the multi-epoch spectra tend to discover short-period binaries, since these systems usually have larger Keplerian velocities. As introduced by Yang et al. (2020), the most spectroscopic binaries (SBs) identified from the LAMOST have an orbital period shorter than 0.6 d. In the next few years, the TMTS is expected to play an important role in providing a large sample with short-period light variations. With the progress of time-domain survey, LAMOST and TMTS observations will give constrains on mass function for a large number of single-lined binaries and thus provide an opportunity for the search of black hole or neutron star binaries.

5.2 Flare stars

As a subclass of eruptive variable star, flare stars are observed to exhibit flaring behaviour during which the brightness of stars dramatically increase within a few minutes and then decrease for several hours. Since the operation of *Kepler* mission, about 3400 stars are found to have flares according to the Q1–Q17 (Data Release 25) long-cadence (LC) data of *Kepler* (Yang & Liu 2019). However, only about 200 flare stars have been identified through its short-cadence (SC) data, since only about 5000 targets in *Kepler* have SC observations (Balona 2015; Yang et al. 2018). Compared to the LC data, the good time resolution of SC data allows further study about the morphology of flares (Balona 2015).

During the high-cadence observations of the LAMOST sky area, TMTS has also captured a series of flare events. Because the flares only cause occasional variations in the light curves, the variability indexes tend to be less sensitive compared with the periodic variations. Therefore, we widened the criterion of $\epsilon_{\frac{1}{\eta}}$ here when identifying flares. On the other hand, the flare search is very dependent on the observational condition since two continuous outliers in a light curve are already enough to produce a flare candidate. It is worth noting that, some spurious 'flares' could be generated when the objects locate on the bad pixels of detectors. These bad pixels usually distort the point spread function of the sources, so the *SExtractor* Flags of the corresponding measurements are very likely non-zero values. Hence, a very tight criterion is needed for the LC quality.

In summary, we searched for the flares in the TMTS-ULC1st light curves using the following criteria: (i) 'daily' flare FDP $<10^{-5}$; (ii) $\epsilon_{\frac{1}{\eta}} > 2.0$; (iii) LC quality = 100 per cent; (iv) excluding bad weather observations. This finally resulted in 356 flare candidates, among which 42 flares were visually confirmed. Among them, 39 flares correspond to *Gaia* sources with both the $G_{\rm BP} - G_{\rm RP}$ colour and the reliable parallax measurement. As shown in Fig. 20, these flare stars are distributed on the lower right branch of the main sequence in the HR diagram, with an absolute magnitude lying between 6.0 and 12.0 mag. Compared to flare stars discovered by other surveys, the 1-min cadence of uninterrupted photometry allows us to further study the shapes and durations (a flare sample is shown in the row v of Fig. 8). In a 5-yr survey plan of TMTS, the discovery number of flares with high-quality light curve coverage is expected to significantly expand the samples of flares with short time resolution.

6 SUMMARY

We present the methodology of variables detecting and preliminary scientific results for the first-year high-cadence monitoring of the LAMOST plates with the TMTS. During the period from 2020 January to 2020 December, the TMTS has observed 188 LAMOST plates and generated 4.9 million uninterrupted light curves for over 4.2 million objects with a cadence of about 1 min. We have applied the inverse von Neumann ratio, LSP, and *Osten*'s methods to detect variability, periodicity, and flares in these light curves, respectively, and then estimated the corresponding significance by their cumulative functions.

A preliminary result of periodicity detection reveals 3723 short-period variable candidates, with a period shorter than 7.5 h. Hence, TMTS is expected to find more than 20 000 short-period periodic variables in a 5-yr observation plan. By plotting the TMTS sources across the HR diagram using the *Gaia* DR2 parameters, we estimated that at least 600 new eclipsing binaries and 800 new δ Scuti stars were discovered in 2020. Furthermore, over 40 flares with great temporal resolution were detected during the observations. Further analysis of the periodic variables and flares will be presented in the forthcoming papers.

ACKNOWLEDGEMENTS

We acknowledge the support of the staffs from Xinglong Observatory of NAOC during the installation, commissioning, and operation of the TMTS system. This work is supported by the Ma Huateng Foundation, the National Natural Science Foundation of China (NSFC grants 12033003 and 11633002), the National Program on Key Research and Development Project (grant no. 2016YFA0400803). XW was also supported by the Scholar Program of Beijing Academy of Science and Technology (BS2020002) and the Strategic Priority Research Program of the Chinese Academy of Sciences, grant no. XDB23040100.

Guoshoujing Telescope (the Large Sky Area Multi-Object Fiber Spectroscopic Telescope LAMOST) is a National Major Scientific Project built by the Chinese Academy of Sciences. Funding for the project has been provided by the National Development and Reform Commission. LAMOST is operated and managed by the National Astronomical Observatories, Chinese Academy of Sciences.

This work has made use of data from the European Space Agency (ESA) mission *Gaia* (https://www.cosmos.esa.int/gaia), processed by the *Gaia* Data Processing and Analysis Consortium (DPAC, https://www.cosmos.esa.int/web/gaia/dpac/consortium). Funding for the DPAC has been provided by national institutions, in particular the institutions participating in the *Gaia* Multilateral Agreement.

This paper includes data collected with the *TESS* mission, obtained from the MAST data archive at the Space Telescope Science Institute (STScI). Funding for the *TESS* mission is provided by the NASA Explorer Program. STScI is operated by the Association of Universities for Research in Astronomy, Inc., under NASA contract NAS 5-26555.

This research has made use of the International Variable Star Index (VSX, Watson et al. 2006) data base, operated at AAVSO, Cambridge, Massachusetts, USA. Some of the results in this paper have been derived using the HEALPIX (Górski et al. 2005) package.

DATA AVAILABILITY

The data underlying this article are subject to an embargo of 10 months from the publication date of the article. However, the data can still be shared on reasonable request to the corresponding author. The light curves from the first-year survey of TMTS will be publicly available at TMTS Public Data Release 1 (in preparation) in 2022.

REFERENCES

Abramowitz M., Stegun I. A., 1972, Handbook of Mathematical Functions. Dover Press, New York
Aigrain S., Parviainen H., Roberts S., Reece S., Evans T., 2017, MNRAS, 471, 759
Alard C., Lupton R. H., 1998, ApJ, 503, 325
Bahramian A. et al., 2017, MNRAS, 467, 2199
Balona L. A., 2015, MNRAS, 447, 2714
Baluev R. V., 2008, MNRAS, 385, 1279
Becker A. C. et al., 2004, ApJ, 611, 418
Bellm E. C. et al., 2019, PASP, 131, 018002
Bertin E., 2006, in Gabriel C., Arviset C., Ponz D., Enrique S., eds, ASP Conf. Ser. Vol. 351, Astronomical Data Analysis Software and Systems XV. Astron. Soc. Pac., San Francisco, p. 112
Bertin E., Arnouts S., 1996, A&AS, 117, 393
Bertin E., Mellier Y., Radovich M., Missonnier G., Didelon P., Morin B., 2002, in Bohlender D. A., Durand D., Handley T. H., eds, ASP Conf. Ser. Vol. 281, Astronomical Data Analysis Software and Systems XI. Astron. Soc. Pac., San Francisco, p. 228
Borucki W. J. et al., 2010, Science, 327, 977
Burdge K. B. et al., 2019, Nature, 571, 528
Burdge K. B. et al., 2020a, ApJ, 905, 32
Burdge K. B. et al., 2020b, ApJ, 905, L7
Chatterjee D., Nugent P. E., Brady P. R., Cannella C., Kaplan D. L., Kasliwal M. M., 2019, ApJ, 881, 128
Chen X., Wang S., Deng L., de Grijs R., Yang M., Tian H., 2020a, ApJS, 249, 18
Chen W.-C., Liu D.-D., Wang B., 2020b, ApJ, 900, L8
Clavel M., Dubus G., Casares J., Babusiaux C., 2021, A&A, 645, A72
Coughlin M. W. et al., 2021, MNRAS, 505, 2954
Cui X.-Q. et al., 2012, Res. Astron. Astrophys., 12, 1197
Downes R. A., Webbink R. F., Shara M. M., Ritter H., Kolb U., Duerbeck H. W., 2001, PASP, 113, 764
Drake A. J. et al., 2009, ApJ, 696, 870
Drake A. J. et al., 2013, ApJ, 763, 32
Drake A. J. et al., 2014a, ApJS, 213, 9
Drake A. J. et al., 2014b, MNRAS, 441, 1186
Drake A. J. et al., 2014c, ApJ, 790, 157
Drake A. J. et al., 2017, MNRAS, 469, 3688
Gaia Collaboration, 2016, A&A, 595, A1
Gaia Collaboration, 2018, A&A, 616, A1
Geier S., 2020, A&A, 635, A193
Geier S., Raddi R., Gentile Fusillo N. P., Marsh T. R., 2019, A&A, 621, A38
Gentile Fusillo N. P. et al., 2019, MNRAS, 482, 4570
Girardi L., Bressan A., Bertelli G., Chiosi C., 2000, A&AS, 141, 371
Gomel R., Faigler S., Mazeh T., 2021a, MNRAS, 501, 2822
Gomel R., Faigler S., Mazeh T., 2021b, MNRAS, 504, 2115
Gomel R., Faigler S., Mazeh T., Pawlak M., 2021c, MNRAS, 504, 5907
Górski K. M., Hivon E., Banday A. J., Wandelt B. D., Hansen F. K., Reinecke M., Bartelmann M., 2005, ApJ, 622, 759
Green G. M., 2018, J. Open Source Softw., 3, 695
Green G. M., Schlafly E., Zucker C., Speagle J. S., Finkbeiner D., 2019, ApJ, 887, 93
Groot P. J. et al., 2003, MNRAS, 339, 427
Gu W.-M. et al., 2019, ApJ, 872, L20
Ho A. Y. Q. et al., 2018, ApJ, 854, L13
Huang F., Li J.-Z., Wang X.-F., Shang R.-C., Zhang T.-M., Hu J.-Y., Qiu Y.-L., Jiang X.-J., 2012, Res. Astron. Astrophys., 12, 1585
Ivezić Ž., Connelly A. J., VanderPlas J. T., Gray A., 2014, Statistics, Data Mining, and Machine Learning in Astronomy. Princeton Univ. Press, Princeton, NJ
Jiménez-Esteban F. M., Torres S., Rebassa-Mansergas A., Skorobogatov G., Solano E., Cantero C., Rodrigo C., 2018, MNRAS, 480, 4505
Kim D.-W., Bailer-Jones C. A. L., 2016, A&A, 587, A18
Kim B., Lépine S., Medan I., 2020, ApJ, 899, 83
Knevitt G., Wynn G. A., Vaughan S., Watson M. G., 2014, MNRAS, 437, 3087
Koch D. G. et al., 2010, ApJ, 713, L79
Kowalski A. F., Hawley S. L., Hilton E. J., Becker A. C., West A. A., Bochanski J. J., Sesar B., 2009, AJ, 138, 633
Kulkarni S. R., Rau A., 2006, ApJ, 644, L63
Kupfer T. et al., 2021, MNRAS, 508, 560
Law N. M. et al., 2009, PASP, 121, 1395
Liu J. et al., 2019, Nature, 575, 618
Liu C. et al., 2020, preprint (arXiv:2005.07210)

Lomb N. R., 1976, Ap&SS, 39, 447
Macfarlane S. A., Toma R., Ramsay G., Groot P. J., Woudt P. A., Drew J. E., Barentsen G., Eislöffel J., 2015, MNRAS, 454, 507
Marsh F. M., Prince T. A., Mahabal A. A., Bellm E. C., Drake A. J., Djorgovski S. G., 2017, MNRAS, 465, 4678
Martínez-Palomera J. et al., 2018, AJ, 156, 186
Masci F. J. et al., 2019, PASP, 131, 018003
Menou K., Narayan R., Lasota J.-P., 1999, ApJ, 513, 811
Miller C. J. et al., 2001, AJ, 122, 3492
Murphy S. J., Hey D., Van Reeth T., Bedding T. R., 2019, MNRAS, 485, 2380
Nidever D. L. et al., 2021, AJ, 161, 192
Ofek E. O., Soumagnac M., Nir G., Gal-Yam A., Nugent P., Masci F., Kulkarni S. R., 2020, MNRAS, 499, 5782
Ofir A. et al., 2010, MNRAS, 404, L99
Osten R. A., Kowalski A., Sahu K., Hawley S. L., 2012, ApJ, 754, 4
Pál A., 2012, MNRAS, 421, 1825
Pala A. F., Ederoclite A., Gänsicke B. T., Gentile Fusillo N. P., Abril J., Raddi R., Vázquez Ramió H., Rebassa-Mansergas A., 2020a, Adv. Space Res., 66, 1235
Pala A. F. et al., 2020b, MNRAS, 494, 3799
Paudel R. R., Gizis J. E., Mullan D. J., Schmidt S. J., Burgasser A. J., Williams P. K. G., Berger E., 2018, ApJ, 858, 55
Paudel R. R., Gizis J. E., Mullan D. J., Schmidt S. J., Burgasser A. J., Williams P. K. G., 2020, MNRAS, 494, 5751
Pelisoli I., Vos J., 2019, MNRAS, 488, 2892
Pietrukowicz P. et al., 2017, Nat. Astron., 1, 0166
Pojmanski G., 2002, Acta Astron., 52, 397
Ramsay G., Hakala P., 2005, MNRAS, 360, 314
Rappaport S., Verbunt F., Joss P. C., 1983, ApJ, 275, 713
Ratzloff J. K., Law N. M., Fors O., Corbett H. T., Howard W. S., del Ser D., Haislip J., 2019, PASP, 131, 075001
Rau A. et al., 2009, PASP, 121, 1334
Ricker G. R. et al., 2014, in Oschmann Jacobus M. J., Clampin M., Fazio G. G., MacEwen H. A., eds, Proc. SPIE Conf. Ser. Vol. 9143, Space Telescopes and Instrumentation 2014: Optical, Infrared, and Millimeter Wave. SPIE, Bellingham, p. 914320
Ricker G. R. et al., 2015, J. Astron. Telesc. Instrum. Syst., 1, 014003
Röser S., Schilbach E., Schwan H., Kharchenko N. V., Piskunov A. E., Scholz R. D., 2008, A&A, 488, 401
Scargle J. D., 1982, ApJ, 263, 835
Shah S., van der Sluys M., Nelemans G., 2012, A&A, 544, A153
Shin M.-S., Sekora M., Byun Y.-I., 2009, MNRAS, 400, 1897
Sokolovsky K. V. et al., 2017, MNRAS, 464, 274
Tamuz O., Mazeh T., Zucker S., 2005, MNRAS, 356, 1466
Thompson T. A. et al., 2019, Science, 366, 637
Tomaney A. B., Crotts A. P. S., 1996, AJ, 112, 2872
Toonen S., Voss R., Knigge C., 2014, MNRAS, 441, 354
VanderPlas J. T., 2018, ApJS, 236, 16
Walkowicz L. M. et al., 2011, AJ, 141, 50
Wang R. et al., 2019, ApJS, 244, 27
Wang B., Chen W., Liu D., Chen H., Wu C., Tang W., Guo Y., Han Z., 2021, MNRAS, 506, 4654
Watson C. L., Henden A. A., Price A., 2006, Society for Astronomical Sciences Annual Symposium, 25, 47
Yang H., Liu J., 2019, ApJS, 241, 29
Yang H., Liu J., Qiao E., Zhang H., Gao Q., Cui K., Han H., 2018, ApJ, 859, 87
Yang F. et al., 2020, ApJS, 249, 31
Yi T., Sun M., Gu W.-M., 2019, ApJ, 886, 97
Zhang K., Bloom J. S., 2021, MNRAS, 505, 515
Zhang J.-C., Ge L., Lu X.-M., Cao Z.-H., Chen X., Mao Y.-N., Jiang X.-J., 2015, PASP, 127, 1292
Zhang J.-C. et al., 2020, PASP, 132, 125001
Zhao G., Zhao Y.-H., Chu Y.-Q., Jing Y.-P., Deng L.-C., 2012, Res. Astron. Astrophys., 12, 723
Zheng L.-L. et al., 2019, AJ, 158, 179
Zhu C.-H., Lü G.-L., Wang Z.-J., 2012, Res. Astron. Astrophys., 12, 1526

This paper has been typeset from a TEX/LATEX file prepared by the author.